J. Fluid Mech. (2023), *vol*. 973, R5, doi:10.1017/jfm.2023.600

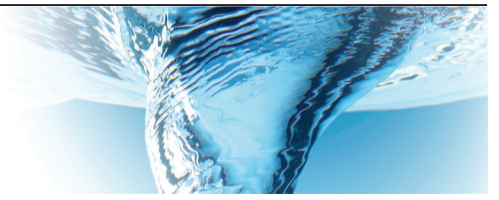

Heat transfer in a quasi-one-dimensional Rayleigh–Bénard convection cell

Lu Zhang[1,2] **and Ke-Qing Xia**[1,2,3,†]

[1]Center for Complex Flows and Soft Matter Research, Southern University of Science and Technology, Shenzhen 518055, PR China

[2]Department of Mechanics and Aerospace Engineering, Southern University of Science and Technology, Shenzhen 518055, PR China

[3]Department of Physics, Southern University of Science and Technology, Shenzhen 518055, PR China

(Received 10 April 2023; revised 8 July 2023; accepted 14 July 2023)

We report an experimental and numerical study on Rayleigh–Bénard convection in a slender rectangular geometry with the aspect ratio Γ varying from 0.05 to 0.3 and a Rayleigh number range of $10^5 \leqslant Ra \leqslant 3 \times 10^9$. The Prandtl number is fixed at $Pr = 4.38$. It is found that the onset of convection is postponed when the convection domain approaches the quasi-one-dimensional limit. The onset Rayleigh number shows a $Ra_c = 328\Gamma^{-4.18}$ scaling for the experiment and a $Ra_c = 810\Gamma^{-3.95}$ scaling for the simulation, both consistent with a theoretical prediction of $Ra_c \sim \Gamma^{-4}$. Moreover, the effective Nusselt–Rayleigh scaling exponent $\beta = \partial(\log Nu)/\partial(\log Ra)$ near the onset of convection also shows a rapid increase with decreasing Γ. Power-law fits to the experimental and numerical data yield $\beta = 0.290\Gamma^{-0.90}$ and $\beta = 0.564\Gamma^{-0.92}$, respectively. Near onset, the flow shows a stretched cell structure. In this regime, the velocity and temperature variations in a horizontal cross-section are found to be almost invariant with height in the core region of a slender domain. As the Rayleigh number increases, the system evolves from the viscous dominant regime to a plume-controlled one, a feature of which is enhancement in the heat transport efficiency. Upon further increase of Ra, the flow comes back to the classical boundary-layer-controlled regime, in which the quasi-one-dimensional geometry has no apparent effect on the global heat transfer.

Key words: Bénard convection, buoyancy-driven instability

1. Introduction

Low dimensionality often leads to the emergence of fascinating physical phenomena and the development of advanced materials, for example, the quantum Hall effect,

† Email address for correspondence: xiakq@sustech.edu.cn

graphene and topological insulators. Reduction of dimensionality is also sometimes desired for effective modelling and efficient simulation. Turbulence, as one of the great unsolved mysteries in classical physics, is three-dimensional (3-D) in nature, and it has an enormous number of degrees of freedom (Frisch 1995). In some circumstances, confinement in one dimension leads to a two-dimensional (2-D) turbulence system, where a novel dual-cascade scenario is predicted and observed (Boffetta & Ecke 2012). Further geometrical confinement leads to a quasi-one-dimensional (quasi-1-D) geometry, for example, a long pipe, an air duct and a deep well. However, turbulent flows in such quasi-1-D geometries are much less explored compared with their 2-D and 3-D counterparts. In this study, we take Rayleigh–Bénard (RB) convection (RBC) as a platform to explore the effect of quasi-1-D geometry on heat transfer.

RBC is a paradigmatic system for the study of thermal convection that occurs widely in nature and in daily life (Ahlers, Grossmann & Lohse 2009; Lohse & Xia 2010; Chillà & Schumacher 2012; Xia 2013). It concerns the flows in an infinite slab of fluid layer that is heated from below and cooled from above. However, most of the existing experiments, numerical simulations and theoretical analyses are carried out in 3-D domains with a finite aspect ratio Γ, which is defined as the ratio between the horizontal scale and vertical scale of the convection domain (with a typical value of about one). Extending the convection domain to large aspect ratio ($\Gamma > 1$) significantly changes the flow structure but has only a minor effect on heat transport (Funfschilling *et al.* 2005; Pandey, Scheel & Schumacher 2018; Stevens *et al.* 2018; Zhu & Zhou 2021).

On the other hand, experiments and simulations conducted in quasi-2-D RB cells reveal a novel flow regime, i.e. the 'plume-controlled' regime (Huang *et al.* 2013; Chong *et al.* 2015; Xia *et al.* 2023), for which the transport properties of the system are controlled by the coherence of thermal plumes rather than the boundary layer. Nevertheless, quasi-1-D RBC is much less explored, in which the increased drag from the lateral sidewall will inevitably change the flow morphology as well as the heat transport behaviour. Until most recently, simulations of quasi-1-D RBC have been conducted as a way of saving computational resources in order to push the Rayleigh number to the highest attainable values (Hartmann *et al.* 2021; Shishkina 2021; Ahlers *et al.* 2022). However, experimental studies on quasi-1-D RBC are rare (Roche *et al.* 2010; de Wit *et al.* 2020), especially for the measurement of heat transfer near the onset of convection, which suffers from severe sidewall heat leakage (Zhang, Chong & Xia 2019).

With the above in mind, in this study, we designed a honeycomb structure that divides a traditional RBC cell into dozens of parallel-connected slender convection domains. Heat transport measurements were carried out for flow states ranging from the onset of convection to fully developed turbulence. We also conducted complementary direct numerical simulations (DNS) to explore the different flow regimes in great detail.

The rest of the paper is organized as follows. In § 2, brief introductions to the experimental and numerical set-ups are provided. Then the main results and discussions are presented in § 3, which is further divided into four subsections. In § 3.1, we present the measured onset Rayleigh numbers as functions of different aspect ratios. The effective *Nu–Ra* scaling after the onset of convection is discussed in § 3.2. In § 3.3, the flow states are explored in more detail using the DNS data. The corresponding heat transfer regimes and the phase diagram are summarized in § 3.4. Finally, we conclude the present work with § 4.

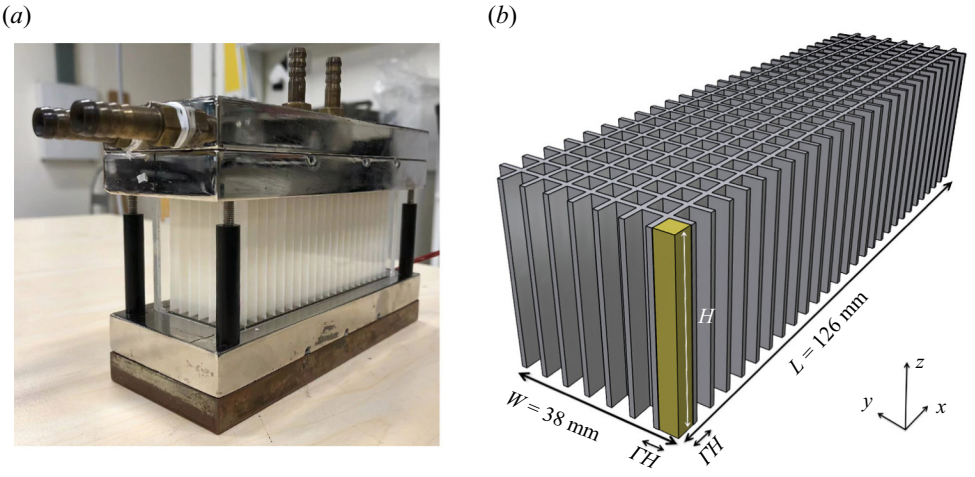

Figure 1. (*a*) Photo of the convection cell. (*b*) Schematic drawing of the 3-D printed structure used in the experiment. The highlighted region shows a single quasi-1-D RB convection domain.

2. Experimental and numerical set-ups

2.1. *Experiments*

In the experiment, a rectangular RB cell with a cross-section of $L \times W = 126$ mm $\times$ 38 mm is used. A quasi-1-D RBC domain is realized by inserting a 3-D printed structure into the convection cell (Zhang & Xia 2023), which divides the original domain into dozens of parallel-connected subdomains (figure 1*a*). The cross-section of the 3-D printed structure is a square lattice, and the lattice spacing equals ΓH (figure 1*b*), where H is the height and Γ is the aspect ratio of the subdomain. The structure is made by a commercial 3-D printer (JG AURORA, Model A8) using a polylactic acid (PLA) filament. The density, thermal conductivity and specific heat capacity of PLA are about 1.2×10^3 kg m^{-3}, 0.15 W (m K)$^{-1}$ and 1.6 kJ (kg K)$^{-1}$, respectively. The outermost sidewall of the convection cell is made of 4 mm thick Plexiglas, whose density, thermal conductivity and specific heat capacity are about 1.2×10^3 kg m^{-3}, 0.21 W (m K)$^{-1}$ and 1.0 kJ (kg K)$^{-1}$. Distilled and deionized water is used as the working fluid and the bulk temperature is set to be 40.0 °C, which corresponds to a Prandtl number of $Pr = 4.38$. So the thermal diffusivities of the sidewall materials and the working fluids are of the same order. Additionally, over 6 cm thick polystyrene foam (whose thermal conductivity is about 0.03 W (m K)$^{-1}$) is wrapped around the outermost sidewall to prevent heat leakage to the surroundings.

For such a configuration, most of the subdomains are isolated from the outermost sidewall, and therefore cannot directly exchange heat with the environment. Using this set-up, we can systematically vary the height H as well as the aspect ratio Γ of a single subdomain and thereby explore the heat transport behaviour in a quasi-1-D RBC domain. Ten sets of structures are fabricated with four different aspect ratios, namely, $\Gamma = 0.05$, 0.1, 0.16 and 0.3. Since the length (L) and width (W) of the convection cell are fixed in the present experiment, and only integral numbers of subdomains are allowed (in both horizontal directions), we have to adjust the thickness of the PLA wall accordingly for specific values of H and ΓH, which turns out to vary from 0.9 mm to 1.2 mm. Moreover, a homemade thermostat whose temperature is set the same as the working fluid

is also applied to minimize sidewall heat leakage. For more details of the heat transfer measurement, readers are referred to Zhang & Xia (2023).

2.2. *Direct numerical simulations*

For a detailed inspection of the velocity and temperature fields in a quasi-1-D RBC domain (see the highlighted region in figure 1*b*), we conduct complementary DNS. The *CUPS* code is adopted to solve the governing equations using a fourth-order finite-volume method on staggered velocity and temperature grids (Chong, Ding & Xia 2018*a*). All boundaries are no-slip and the sidewalls are set to be adiabatic. The possible sidewall effect (Wan *et al.* 2019) and thermal coupling effect between adjacent subdomains in the experiment are not considered for the sake of simplicity.

3. Results and discussions

Figures 2(*a*) and 2(*b*) show the *Nu*–*Ra* relations for four different aspect ratios obtained by experiment and DNS, respectively. For comparison, data obtained in cells with aspect ratios of unity are plotted as well. The error bars (taken as one standard deviation of the measured Nusselt number time series) are within the size of a symbol and therefore not shown. It is seen that the experimental and numerical results show qualitatively good agreement. Firstly, the onset of convection (the intersection point of the *Nu*–*Ra* curve with the dashed horizontal line of $Nu = 1$) is considerably postponed as the cell approaches the quasi-1-D limit ($\Gamma \ll 1$). Secondly, the effective local *Nu*–*Ra* scaling exponent ($\beta = \partial(\log Nu)/\partial(\log Ra)$) just after the onset of convection shows a rapid increase with decreasing Γ. Finally, when the Rayleigh number is large enough, the experimental and numerical data points with different aspect ratios all collapse onto the black solid curves, which represent the predictions of the Grossmann–Lohse (GL) theory (Grossmann & Lohse 2000, 2001, 2002; Stevens *et al.* 2013). We discuss these features in detail below.

3.1. *The onset Rayleigh number Ra_c*

Figure 3(*a*) shows the log–log plot of the onset Rayleigh number Ra_c as a function of the aspect ratio Γ. The red stars and blue squares denote the experimental and numerical data of the present study, respectively. We also plot the critical Rayleigh numbers obtained from the literature (Catton & Edwards 1970; Muller, Neumann & Weber 1984; Hébert *et al.* 2010). It is seen that all the data points fall onto a solid curve with $Ra_c = (2\pi)^4(1 + \Gamma^{-2})(1 + \Gamma^{-2}/2)$, which is derived by Shishkina (2021) for a rectangular cell with an adiabatic sidewall. In the quasi-1-D limit ($\Gamma \ll 1$), the above equation reduces to $Ra_c = 8\pi^4\Gamma^{-4}$. Power-law fits to the present experimental and numerical data yield $Ra_c = 328\Gamma^{-4.18}$ and $Ra_c = 810\Gamma^{-3.95}$ (the solid lines in the inset of figure 3*a*), which are both consistent with the theoretical prediction above. To the best of our knowledge, this is the first experimental result of the $Ra_c \sim \Gamma^{-4}$ scaling in the quasi-1-D regime.

Though the negative biquadratic power law obtained in a quasi-1-D RBC domain is in sharp contrast with its quasi-2-D counterpart $Ra_c \sim \Gamma^{-2}$ (Chong & Xia 2016), it is worth noting that it has the same form as the onset Rayleigh number of rotating Rayleigh–Bénard convection (RRBC), which scales as $Ra_c \sim Ek^{-4/3} \sim (l/H)^{-4}$, where *Ek* is the Ekman number, which quantifies the strength of rotation, and *l* is the horizontal

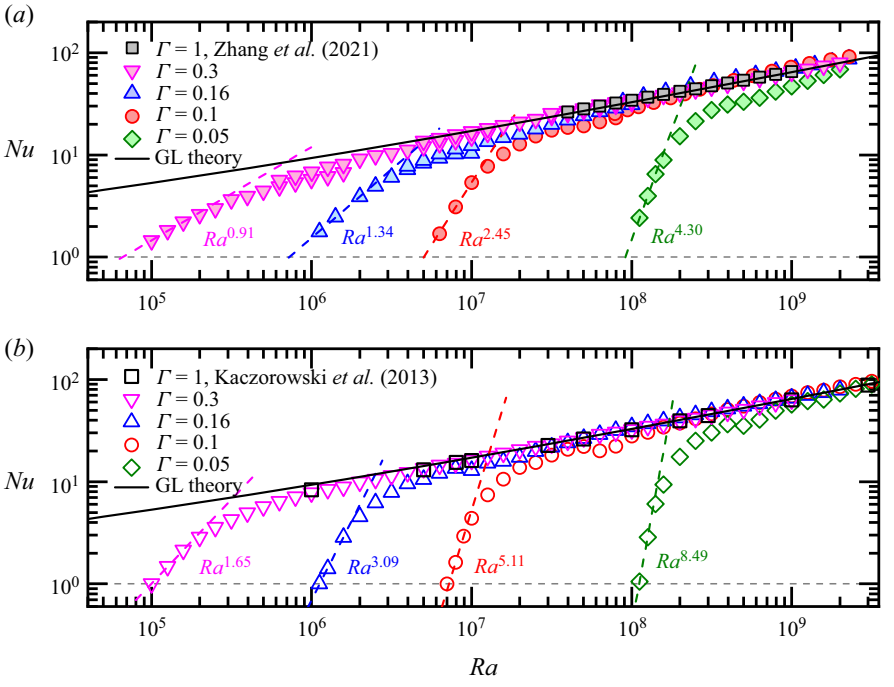

Figure 2. (*a*) The experimentally measured *Nu* versus *Ra* data for RBC domains with different aspect ratios. (*b*) The corresponding *Nu*–*Ra* relations obtained by DNS. The dashed lines in both panels show power-law fits to the data points near onset, and the solid lines represent predictions of the GL theory.

scale of convection near onset. This also suggests that applying geometrical constraint and dynamical constraint to thermal convection may share the same underlying mechanism for the changes in heat transport properties (Chong *et al.* 2017; Lim *et al.* 2019; Xia *et al.* 2023).

3.2. *The Nu–Ra scaling near onset*

Another striking feature of the heat transfer in a quasi-1-D RBC domain is that the *Nu*–*Ra* curve shows a steep slope on a log–log plot near the onset Rayleigh number. Such behaviour can be described quantitatively by an effective scaling exponent β, which is obtained by applying a power-law fit to the near-onset data points (see the dashed lines in figure 2*b*). It is seen that the corresponding local scaling exponent β increases rapidly with decreasing aspect ratio. For the lowest aspect ratio explored in this study ($\Gamma = 0.05$), the local scaling exponent is $\beta = 4.30$ for the experiment and $\beta = 8.49$ for the DNS. Stevens, Lohse & Verzicco (2014) conducted a systematic DNS to explore the effects of different sidewall temperature boundary conditions in a single RBC domain. They found that the heat transfer efficiencies for an isothermal sidewall boundary condition and an adiabatic condition can differ by over 10 % at a Rayleigh number of 2×10^8. The Nusselt numbers for cells with finite sidewall thicknesses are in between the above two ideal cases – see figure 9 in Stevens *et al.* (2014). A possible reason for the discrepancy in β is the different sidewall thermal boundary conditions: most of the quasi-1-D subdomains in the experiment are thermally coupled with their nearest neighbours, while the DNS assumes that the sidewall is adiabatic.

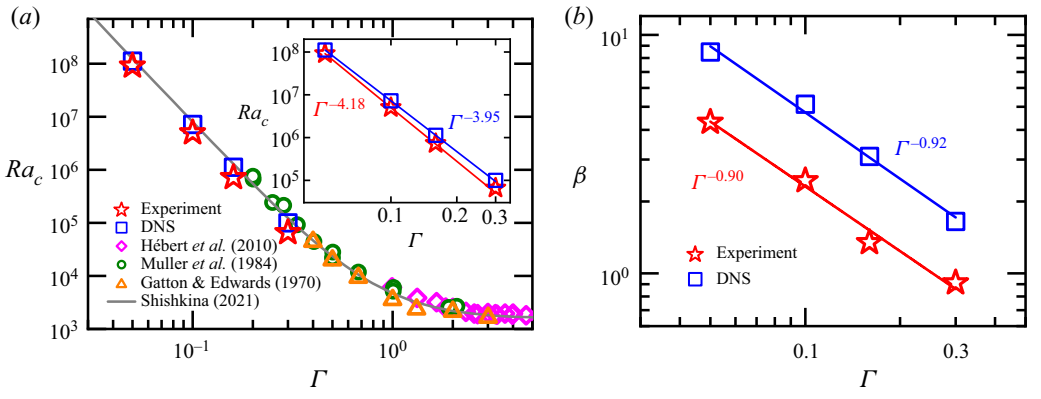

Figure 3. (*a*) The onset Rayleigh number Ra_c as a function of the aspect ratio Γ. Red stars are the experimental data and blue squares are obtained by DNS. The grey solid curve shows the theoretical prediction of $Ra_c = (2\pi)^2(1+\Gamma^{-2})(1+\Gamma^{-2}/2)$ proposed by Shishkina (2021). Data from references are also plotted for comparison. The red and blue solid lines in the inset show power-law fits with $Ra_c = 328\Gamma^{-4.18}$ and $Ra_c = 810\Gamma^{-3.95}$, respectively. (*b*) The effective near-onset Nusselt–Rayleigh scaling exponent β as a function of the aspect ratio Γ. The legend is the same as for panel (a). The red and blue solid lines show power-law fits with $0.290\Gamma^{-0.90}$ and $0.564\Gamma^{-0.92}$, respectively.

Figure 3(*b*) show the β–Γ relations obtained from figure 2. Power-law fits to the data yield $\beta = 0.290\Gamma^{-0.90}$ for the experiment and $\beta = 0.564\Gamma^{-0.92}$ for the DNS, respectively. Similar behaviour of heat transport is also observed in RRBC: for a rapidly rotating cell, the effective near-onset local *Nu*–*Ra* scaling exponent also shows a rapid increase with decreasing Ekman number (Cheng *et al.* 2015; Plumley & Julien 2019). It is also worth mentioning that in our quasi-1-D RBC configuration, the extremely rapid increase of *Nu* serves to divide the flow roughly into two states: before onset the system is in a 'thermal insulating' state, in which heat is transported by conduction only; after onset the system turns into a 'thermal conducting' state, in which heat is transferred efficiently by turbulent convection. In this sense, the present system can be viewed as a 'convective thermal diode' (Wehmeyer *et al.* 2017), which might be used for advanced thermal control or other engineering applications.

In figures 4(*a*) and 4(*b*), we present the compensated plots of $(Nu-1)/Ra_c^{1/3}$ versus Ra/Ra_c obtained from the experiment and DNS, respectively. For comparison, Nusselt numbers measured near the convective onset in a cylindrical cell with $\Gamma = 2$ (Behringer & Ahlers 1982) were also plotted in figure 4(*a*). It is seen that the curves with different aspect ratios basically collapse onto a single master curve even for the near-onset regime, where the effective scaling exponent shows a gradual transition to the classical value of 1/3 within one decade of the reduced Rayleigh number Ra/Ra_c. Though an explicit explanation for this universal behaviour is not yet available, we hope that a theoretical understanding will come up in the near future. Experimentally, it would also be quite interesting to push Γ to even smaller values to see whether the near-onset local *Nu*–*Ra* scaling exponent will increase further or not.

3.3. *The near-onset flow structure*

Figure 5(*a*) shows the streamlines obtained by DNS for different aspect ratios. The Rayleigh number is fixed at $Ra = 1.1Ra_c$. It is seen that a feature of the flow is an

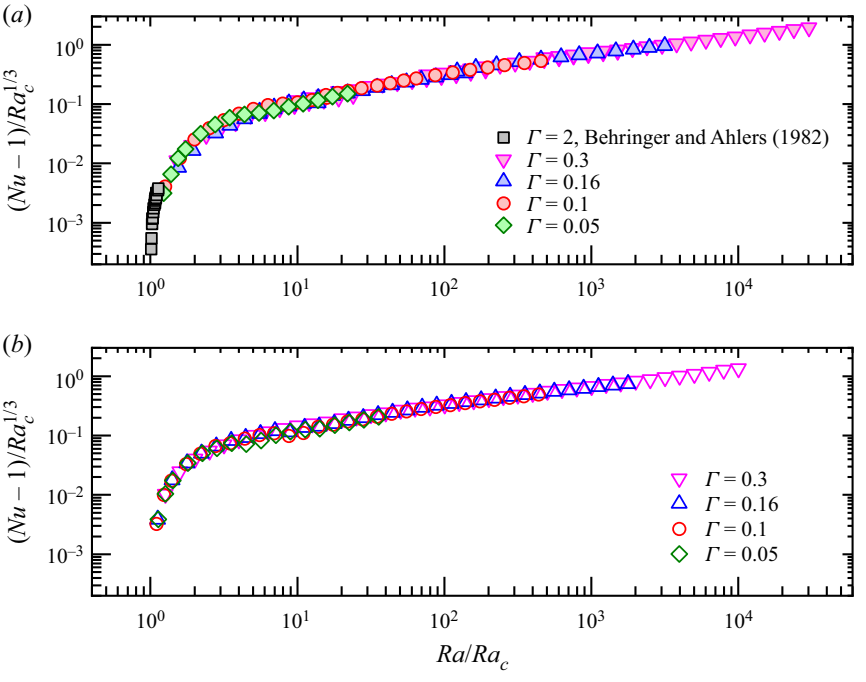

Figure 4. Compensated plots of $(Nu-1)/Ra_c^{1/3}$ versus Ra/Ra_c for (a) the experimental data and (b) the numerical data.

elongated, stretched cell structure. It consists of a hot, ascending flow on one side and a cold, descending flow on the other side. Figures 5(b) and 5(c) show vertical profiles of the root mean square (r.m.s.) temperature $\langle (T-\langle T\rangle_{x,y})^2\rangle_{x,y}^{1/2}$ and the r.m.s. vertical velocity $\langle w^2\rangle_{x,y}^{1/2}$, respectively. Here $\langle\cdot\rangle_{x,y}$ denotes averaging over a certain horizontal plane. It is seen that the two profiles have almost the same shape, which is in line with the prediction that the temperature variation and vertical velocity are highly correlated when the nonlinearity effect is weak (Chandrasekhar 1961).

With these facts, the above $Ra_c \sim \Gamma^{-4}$ scaling, which was recently derived by Shishkina (2021) and Ahlers *et al.* (2022), can also be understood in a different way as follows. We start with the exact balance between dissipation and global heat transfer. If we denote by δ_w and δ_T the typical vertical velocity and temperature scales of the ascending/descending flow observed in figure 5(a), then the exact relations for viscous dissipation and thermal dissipation in the near-onset regime ($Ra \to Ra_c$) read

$$\epsilon_u = \frac{\nu^3}{H^4} Pr^{-2} Ra_c (Nu-1) \sim \nu \left(\frac{\delta_w}{\Gamma H}\right)^2, \tag{3.1}$$

$$\epsilon_T = \kappa \frac{\Delta^2}{H^2} Nu \sim \kappa \left(\frac{\delta_T}{\Gamma H}\right)^2 + \kappa \frac{\Delta^2}{H^2}. \tag{3.2}$$

Moreover, considering the fact that the temperature and velocity fields are highly correlated, the Nusselt number can also be expressed as

$$Nu - 1 \sim \frac{\delta_w \delta_T}{\kappa \Delta / H}. \tag{3.3}$$

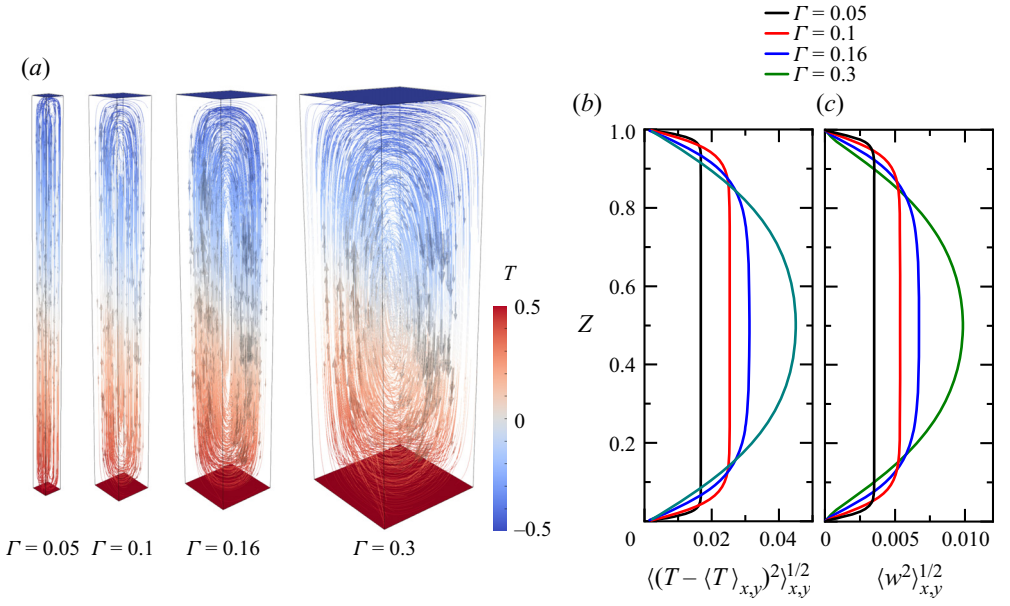

Figure 5. (*a*) Streamlines in the near-onset regime $Ra/Ra_c = 1.1$ for different aspect ratios, with different colours showing the local temperatures. (*b*) Vertical profiles of the temperature variations for different aspect ratios. (*c*) The corresponding profiles of the vertical velocity variations.

Moving the last term in (3.2) to the left-hand side yields $\kappa(\Delta/H)^2(Nu-1) \sim \kappa[\delta_T/(\Gamma H)]^2$. If we now multiply this by (3.1), and then substitute the term $Nu-1$ with (3.3), we can obtain

$$Ra_c \sim \Gamma^{-4}. \tag{3.4}$$

It is also worth mentioning that, for a quasi-2-D RBC domain (Chong & Xia 2016), (3.1) is still valid, whereas (3.2) should be replaced by $\epsilon_T = \kappa(\Delta/H)^2 Nu \sim \kappa(\delta_T/H)^2 + \kappa(\Delta/H)^2$. We can then obtain $Ra_c \sim \Gamma^{-2}$, which is in agreement with the scaling derived using linear stability analysis (Bizon *et al.* 1997).

Another interpretation for the $Ra_c \sim \Gamma^{-4}$ scaling originates from linear stability analysis. Suppose that the vertical velocity perturbation near onset has the form $w = W(z)\exp[\mathrm{i}(k_x x + k_y y)]$. It should satisfy the following sixth-order ordinary differential equation (Chandrasekhar 1961):

$$\left(\frac{\partial^2}{\partial z^2} - k^2H^2\right)^3 W = -Ra(kH)^2 W, \tag{3.5}$$

where $k = \sqrt{k_x^2 + k_y^2}$ is the wavenumber. For the present system, the no-slip boundary condition requires that $kH \sim \Gamma^{-1}$. As shown in figure 5(*b*), the r.m.s. vertical velocity does not exhibit any appreciable change in the core region of the quasi-1-D cell, which implies that $\partial^n W/\partial z^n = 0$. Substituting this (assuming it holds up to sixth order) into (3.5) again results in $Ra \sim (kH)^4 \sim \Gamma^{-4}$.

We remark that it is quite surprising that the typical temperature and velocity scales are both invariant with height in a quasi-1-D cell. This feature is neither predicted by the exact solution of the velocity profile in a horizontally unconstrained domain (Chandrasekhar

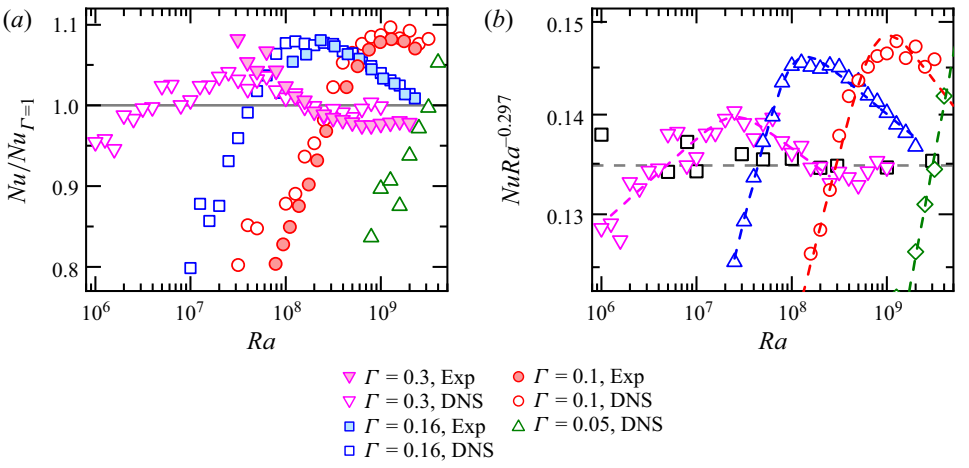

Figure 6. (*a*) The normalized Nusselt number $Nu/Nu_{\Gamma=1}$ as functions of Rayleigh number for different aspect ratios. Solid symbols show the experimental data and open symbols are obtained by DNS. (*b*) Compensated plot of the *Nu*–*Ra* relations taken from DNS. The dashed lines show fits with a transition function $f(Ra) = ARa^{\alpha_2}[1 + (Ra_0/Ra)^4]^{(\alpha_2-\alpha_1)/4}$.

1961), nor described by the eigenmodes of the Laplace operator (Shishkina 2021). Nevertheless, this feature reminds us of the Taylor–Proudman theorem, which states that, for a rapidly rotating convection system, the velocity will be uniform along any line parallel to the axis of rotation. The Taylor–Proudman theorem implies a balance between the Coriolis force and the pressure gradient in RRBC, while the dominant force balance in a quasi-1-D RBC cell is between viscous force and buoyancy.

3.4. *Different heat transfer regimes and the phase diagram*

Figures 6(*a*) and 6(*b*) show the normalized and compensated Nusselt numbers as functions of Rayleigh number, respectively. The *Nu*–*Ra* relations measured in cells with unity aspect ratio ($\Gamma = 1$) are taken as benchmarks for the normalization (see the solid and open squares in figure 2). Power-law fits to these data yield $Nu_{\Gamma=1} = 0.192Ra^{0.282}$ for the experiment (Zhang, Ding & Xia 2021) and $Nu_{\Gamma=1} = 0.135Ra^{0.297}$ for the DNS (Kaczorowski & Xia 2013). It is seen that heat transfer enhancement is achieved for all four aspect ratios providing the Rayleigh number exceeds a certain threshold value. For the parameter range explored, maximum heat transfer enhancement is observed for $\Gamma = 0.1$ at $Ra = 1.3 \times 10^9$, which is about 10 %. This is in agreement with the recent numerical simulations of Hartmann *et al.* (2021).

For a quantitative determination of the heat transfer enhancement regime, we use the transition function $f(Ra) = ARa^{\alpha_2}[1 + (Ra_0/Ra)^4]^{(\alpha_2-\alpha_1)/4}$ to fit the DNS data, where A, α_1, α_2 and Ra_0 are four independent fitting parameters. When $Ra \ll Ra_0$, the function above approaches $f(Ra) \approx ARa_0^{\alpha_2-\alpha_1}Ra^{\alpha_1}$; while in the limit of $Ra \gg Ra_0$, it reduces to $f(Ra) \approx ARa^{\alpha_2}$. Therefore, such a functional form can be adopted to describe the transition between two power laws, and the fitting parameter Ra_0 can be interpreted as a transitional Rayleigh number. The fits are carried out to the numerical data points shown in figure 6(*b*). For the case of $\Gamma = 0.3$, the fitting is only done with data points up to $Ra = 2 \times 10^8$, beyond which the data converge to the case of $\Gamma = 1$. The fitting results are plotted as dashed curves in figure 6(*b*). The parameters are listed in table 1. When $\alpha_1 = \alpha_2$, the function above is identical to a power law. The range of the heat transfer enhancement

Γ	A	α_1	α_2	Ra_0	Ra_{t1}	Ra_{t2}
1	0.135	0.297	0.297	—	—	—
0.3	0.208	0.325	0.274	2.45×10^7	5.12×10^6	1.68×10^8
0.16	0.237	0.421	0.272	9.58×10^7	4.46×10^7	3.28×10^9
0.1	0.349	0.417	0.256	7.86×10^8	2.98×10^8	1.41×10^{10}
0.05	0.00374	0.461	0.461	—	3.08×10^9	—

Table 1. Fitting parameters and the corresponding transition Rayleigh numbers.

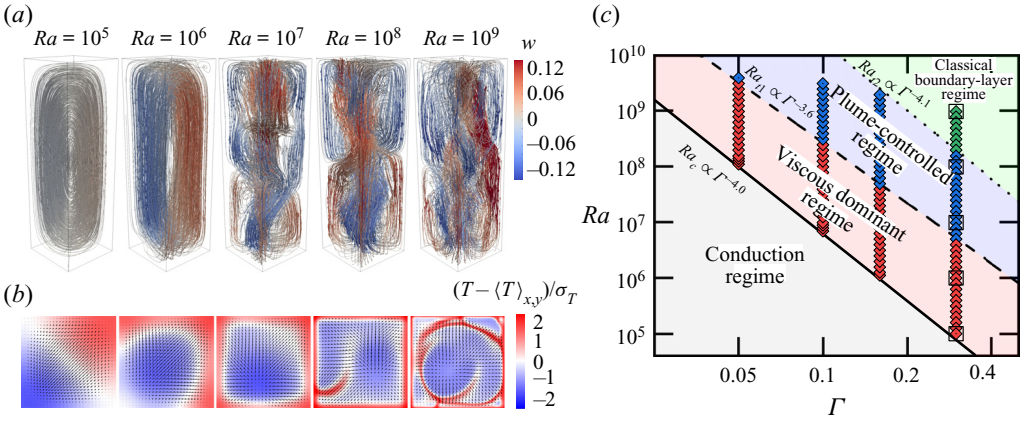

Figure 7. (*a*) Streamlines at different Rayleigh numbers in a $\Gamma = 0.3$ convection domain, with different colours showing the magnitude of the vertical velocity. (*b*) Snapshots of temperature fluctuations $(T - \langle T\rangle_{x,y})/\sigma_T$ in a horizontal cross-section located at one thermal boundary-layer thickness away from the bottom plate. (*c*) Phase diagram of different heat transport regimes in a slender RBC domain. The Prandtl number is fixed at $Pr = 4.38$. The open squares correspond to the positions of the snapshots shown in panels (*a*) and (*b*).

regime (Ra_{t1}, Ra_{t2}) is then determined by the intersection points of the dashed curves and the solid line. Fitting Ra_{t1} and Ra_{t2} with power laws of Γ yield $Ra_{t1} \sim \Gamma^{-3.6}$ and $Ra_{t2} \sim \Gamma^{-4.1}$, respectively.

Next, we plot in figure 7(*a*) the flow fields at different Rayleigh numbers in a $\Gamma = 0.3$ cell. Near onset ($Ra = 10^5$), the flow is static and exhibits a stretched cell structure, as mentioned above. With increasing Rayleigh number ($Ra = 10^6$), the flow is strengthened and corner flows are gradually developed. A further increase in Ra breaks the stretched cell structure and the flow eventually becomes turbulent. In this regime, thermal plumes are generated in the corners of the cell and then emitted into the bulk region. Thereafter, they merge and condense into a highly coherent giant plume, and then impinge on the opposite plate, thus facilitating efficient heat transport. This heat transfer enhancement regime is also known as the 'plume-controlled' regime (Xia *et al.* 2023). The transition in flow state is also reflected in the thermal boundary-layer behaviour.

Figure 7(*b*) shows snapshots of the normalized temperature fields $(T - \langle T\rangle_{x,y})/\sigma_T$ in a horizontal cross-section that is located at $z = 1/(2Nu)$ (one thermal boundary-layer thickness away from the bottom plate), where σ_T is the r.m.s. temperature in that plane. As the Rayleigh number increases, the symmetry of the flow breaks down. Hot plumes are developed in the corner region and a giant cold plume is formed in the centre of the plane (Chong *et al.* 2015). Further increase in Ra will squeeze the hot flows to the

peripheral of the cell. Meanwhile, sheet-like plumes are gradually developed in the centre of the domain (Zhou & Xia 2010), which indicates that the flow enters the classical boundary-layer-controlled regime. In this regime, the heat transfer efficiency shows no apparent aspect-ratio dependence (see figure 6*b*).

With the results above, we map out in figure 7(*c*) the phase diagram of the heat transport properties for quasi-1-D RBC, with the solid diamonds representing the DNS data. Four regimes are identified, namely, the classical boundary-layer-controlled regime, the plume-controlled regime, the viscous dominant regime and finally the conduction regime. The boundaries separating the different regimes are almost parallel to each other and show power-law scalings close to Γ^{-4}, which are much steeper than those found in a quasi-2-D domain (Chong & Xia 2016). It is also worth mentioning that the Prandtl number may also have a significant effect on the phase diagram (Chong *et al.* 2018*b*; Hartmann *et al.* 2021), which, of course, deserves further investigation.

4. Conclusions

To conclude, we have made a systematic study of the heat transport properties and flow states in a quasi-1-D RBC cell. The experiments were conducted using a meticulously designed 3-D printed structure. Our results provide the first experimental evidence for the $Ra_c \sim \Gamma^{-4}$ scaling in the quasi-1-D regime ($0.05 \leqslant \Gamma \leqslant 0.3$), which is also consistent with recent theoretical predictions and numerical simulations (Shishkina 2021; Ahlers *et al.* 2022). In addition, the effective local *Nu*–*Ra* scaling exponent just after the onset of convection shows a rapid increase with decreasing aspect ratio as $\beta \sim \Gamma^{-0.90}$. Subsequent DNS confirm this experimental finding. The discrepancies in the magnitudes of Ra_c and β obtained from experiments and simulations are most likely caused by the different lateral thermal boundary conditions. However, despite this difference, both experiment and DNS results show the same flow physics with respect to the heat transport properties.

Our DNS also reveals that the flow in a quasi-1-D RBC cell shows a stretched cell structure near onset and that the typical velocity and temperature scales are invariant with height in the core region of the cell. Based on these findings, we provide several interpretations of the observed $Ra_c \sim \Gamma^{-4}$ scaling. Finally, different heat transfer regimes are identified and the corresponding phase diagram is mapped out.

The results of this study suggest that quasi-1-D RBC may be utilized for advanced thermal engineering applications like thermal diodes, thermal regulators and efficient heat exchangers. We also remark that the effect of Prandtl number, as well as a comprehensive theoretical understanding for the heat transfer behaviour in quasi-1-D RBC, remain open questions and call for future studies.

Acknowledgements. We thank Dr Y.-C. Xie and Mr L. Ren for fruitful discussions, and gratefully acknowledge support of this work by the Center for Computational Science and Engineering of Southern University of Science and Technology.

Funding. This work is supported by the National Natural Science Foundation of China (nos. 12202173, 92152104, 12072144 and 12232010) and the Center for Computational Science and Engineering of Southern University of Science and Technology.

Declaration of interests. The authors report no conflict of interest.

Author ORCIDs.
Lu Zhang https://orcid.org/0000-0003-4009-2969;
Ke-Qing Xia https://orcid.org/0000-0001-5093-9014.

References

Ahlers, G., Grossmann, S. & Lohse, D. 2009 Heat transfer and large scale dynamics in turbulent Rayleigh–Bénard convection. *Rev. Mod. Phys.* **81** (2), 503–537.

Ahlers, G., Bodenschatz, E., Hartmann, R., He, X.-Z., Lohse, D., Reiter, P., Stevens, R.J.A.M., Verzicco, R., Wedi, M., Weiss, S., *et al.* 2022 Aspect ratio dependence of heat transfer in a cylindrical Rayleigh–Bénard cell. *Phys. Rev. Lett.* **128** (8), 084501.

Behringer, R.P. & Ahlers, G. 1982 Heat-transport and temporal evolution of fluid-flow near the Rayleigh–Bénard instability in cylindrical containers. *J. Fluid Mech.* **125**, 219–258.

Bizon, C., Werne, J., Predtechensky, A.A., Julien, K., McCormick, W.D., Swift, J.B. & Swinney, H.L. 1997 Plume dynamics in quasi-2D turbulent convection. *Chaos* **7** (1), 107–124.

Boffetta, G. & Ecke, R.E. 2012 Two-dimensional turbulence. *Annu. Rev. Fluid Mech.* **44** (1), 427–451.

Catton, I. & Edwards, D.K. 1970 Initiation of thermal convection in finite right circular cylinders. *AIChE J.* **16** (4), 594–601.

Chandrasekhar, S. 1961 *Hydrodynamic and Hydromagnetic Stability*. Oxford University Press.

Cheng, J.S., Stellmach, S., Ribeiro, A., Grannan, A., King, E.M. & Aurnou, J.M. 2015 Laboratory-numerical models of rapidly rotating convection in planetary cores. *Geophys. J. Intl* **201** (1), 1–17.

Chillà, F. & Schumacher, J. 2012 New perspectives in turbulent Rayleigh–Bénard convection. *Eur. Phys. J.* E **35** (7), 58.

Chong, K.-L., Ding, G.-Y. & Xia, K.-Q. 2018*a* Multiple-resolution scheme in finite-volume code for active or passive scalar turbulence. *J. Comput. Phys.* **375**, 1045–1058.

Chong, K.L., Huang, S.D., Kaczorowski, M. & Xia, K.Q. 2015 Condensation of coherent structures in turbulent flows. *Phys. Rev. Lett.* **115** (26), 264503.

Chong, K.-L., Wagner, S., Kaczorowski, M., Shishkina, O. & Xia, K.-Q. 2018*b* Effect of Prandtl number on heat transport enhancement in Rayleigh–Bénard convection under geometrical confinement. *Phys. Rev. Fluids* **3** (1), 013501.

Chong, K.-L. & Xia, K.-Q. 2016 Exploring the severely confined regime in Rayleigh–Bénard convection. *J. Fluid Mech.* **805**, R4.

Chong, K.-L., Yang, Y.-T., Huang, S.-D., Zhong, J.-Q., Stevens, R.J.A.M., Verzicco, R., Lohse, D. & Xia, K.-Q. 2017 Confined Rayleigh–Bénard, rotating Rayleigh–Bénard, and double diffusive convection: a unifying view on turbulent transport enhancement through coherent structure manipulation. *Phys. Rev. Lett.* **119**, 064501.

Frisch, U. 1995 *Turbulence: The Legacy of A. N. Kolmogorov*. Cambridge University Press.

Funfschilling, D., Brown, E., Nikolaenko, A. & Ahlers, G. 2005 Heat transport by turbulent Rayleigh–Bénard convection in cylindrical samples with aspect ratio one and larger. *J. Fluid Mech.* **536**, 145–154.

Grossmann, S. & Lohse, D. 2000 Scaling in thermal convection: a unifying theory. *J. Fluid Mech.* **407**, 27–56.

Grossmann, S. & Lohse, D. 2001 Thermal convection for large Prandtl numbers. *Phys. Rev. Lett.* **86**, 3316–3319.

Grossmann, S. & Lohse, D. 2002 Prandtl and Rayleigh number dependence of the Reynolds number in turbulent thermal convection. *Phys. Rev.* E **66**, 016305.

Hartmann, R., Chong, K.-L., Stevens, R.J.A.M., Verzicco, R. & Lohse, D. 2021 Heat transport enhancement in confined Rayleigh–Bénard convection feels the shape of the container. *Europhys. Lett.* **135** (2), 24004.

Hébert, F., Hufschmid, R., Scheel, J. & Ahlers, G. 2010 Onset of Rayleigh–Bénard convection in cylindrical containers. *Phys. Rev.* E **81** (4), 046318.

Huang, S.-D., Kaczorowski, M., Ni, R. & Xia, K.-Q. 2013 Confinement-induced heat-transport enhancement in turbulent thermal convection. *Phys. Rev. Lett.* **111**, 104501.

Kaczorowski, M. & Xia, K.-Q. 2013 Turbulent flow in the bulk of Rayleigh–Bénard convection: small-scale properties in a cubic cell. *J. Fluid Mech.* **722**, 596–617.

Lim, Z.-L., Chong, K.-L., Ding, G.-Y. & Xia, K.-Q. 2019 Quasistatic magnetoconvection: heat transport enhancement and boundary layer crossing. *J. Fluid Mech.* **870**, 519–542.

Lohse, D. & Xia, K.-Q. 2010 Small-scale properties of turbulent Rayleigh–Bénard convection. *Annu. Rev. Fluid Mech.* **42** (1), 335–364.

Muller, G., Neumann, G. & Weber, W. 1984 Natural-convection in vertical Bridgman configurations. *J. Cryst.* **70** (1–2), 78–93.

Pandey, A., Scheel, J.D. & Schumacher, J. 2018 Turbulent superstructures in Rayleigh–Bénard convection. *Nat. Commun.* **9** (1), 2118.

PLUMLEY, M. & JULIEN, K. 2019 Scaling laws in Rayleigh–Bénard convection. *Earth Space Sci.* **6** (9), 1580–1592.

ROCHE, P.E., GAUTHIER, F., KAISER, R. & SALORT, J. 2010 On the triggering of the ultimate regime of convection. *New J. Phys.* **12** (8), 085014.

SHISHKINA, O. 2021 Rayleigh–Bénard convection: the container shape matters. *Phys. Rev. Fluids* **6**, 090502.

STEVENS, R.J.A.M., BLASS, A., ZHU, X.-J., VERZICCO, R. & LOHSE, D. 2018 Turbulent thermal superstructures in Rayleigh–Bénard convection. *Phys. Rev. Fluids* **3** (4), 041501(R).

STEVENS, R.J.A.M., LOHSE, D. & VERZICCO, R. 2014 Sidewall effects in Rayleigh–Bénard convection. *J. Fluid Mech.* **741**, 1–27.

STEVENS, R.J.A.M., VAN DER POEL, E.P., GROSSMANN, S. & LOHSE, D. 2013 The unifying theory of scaling in thermal convection: the updated prefactors. *J. Fluid Mech.* **730**, 295–308.

WAN, Z.-H., WEI, P., VERZICCO, R., LOHSE, D., AHLERS, G. & STEVENS, R.J.A.M. 2019 Effect of sidewall on heat transfer and flow structure in Rayleigh–Bénard convection. *J. Fluid Mech.* **881**, 218–243.

WEHMEYER, G., YABUKI, T., MONACHON, C., WU, J.-Q. & DAMES, C. 2017 Thermal diodes, regulators, and switches: physical mechanisms and potential applications. *Appl. Phys. Rev.* **4** (4), 041304.

DE WIT, X.M., AGUIRRE GUZMÁN, A.J., MADONIA, M., CHENG, J.S., CLERCX, H.J.H. & KUNNEN, R.P.J. 2020 Turbulent rotating convection confined in a slender cylinder: the sidewall circulation. *Phys. Rev. Fluids* **5** (2), 023502.

XIA, K.-Q. 2013 Current trends and future directions in turbulent thermal convection. *Theor. Appl. Mech.* **3** (5), 052001.

XIA, K.-Q., HUANG, S.-D., XIE, Y.-C. & ZHANG, L. 2023 Tuning heat transport via coherent structure manipulation: recent advances in thermal turbulence. *Nat. Sci. Rev.* **10** (6), Nwad012.

ZHANG, L., CHONG, K.-L. & XIA, K.-Q. 2019 Moisture transfer by turbulent natural convection. *J. Fluid Mech.* **874**, 1041–1056.

ZHANG, L., DING, G.-Y. & XIA, K.-Q. 2021 On the effective horizontal buoyancy in turbulent thermal convection generated by cell tilting. *J. Fluid Mech.* **914**, A15.

ZHANG, L. & XIA, K.-Q. 2023 Achieving heat transfer enhancement via manipulation of bulk flow structures in turbulent thermal convection. *Phys. Rev. Fluids* **8** (2), 023501.

ZHOU, Q. & XIA, K.-Q. 2010 Physical and geometrical properties of thermal plumes in turbulent Rayleigh–Bénard convection. *New J. Phys.* **12** (7), 075006.

ZHU, X. & ZHOU, Q. 2021 Flow structures of turbulent Rayleigh–Bénard convection in annular cells with aspect ratio one and larger. *Acta Mechanica Sin.* **37** (8), 1291–1298.